ELSEVIER

Contents lists available at ScienceDirect

Journal of Structural Biology

journal homepage: www.elsevier.com/locate/yjsbi



Correlative imaging reveals physiochemical heterogeneity of microcalcifications in human breast carcinomas



Jennie A.M.R. Kunitake^a, Siyoung Choi^b, Kayla X. Nguyen^c, Meredith M. Lee^a, Frank He^b, Daniel Sudilovsky^{d,e}, Patrick G. Morris^f, Maxine S. Jochelson^g, Clifford A. Hudis^f, David A. Muller^{c,h}, Peter Fratzlⁱ, Claudia Fischbach^{b,h,*}, Admir Masic^{l,*}, Lara A. Estroff^{a,h,*}

- ^a Department of Materials Science and Engineering, Cornell University, Ithaca, NY 14853, USA
- ^b Nancy E. and Peter C. Meinig School of Biomedical Engineering, Cornell University, Ithaca, NY 14853, USA
- ^c School of Applied and Engineering Physics, Cornell University, Ithaca, NY 14853, USA
- d Department of Pathology and Laboratory Medicine, Cayuga Medical Center at Ithaca, Ithaca, NY 14850, USA
- ^e Department of Pathology, Upstate Medical University, SUNY, Binghamton, NY 13904, USA
- Freast Medicine Service, Department of Medicine, Memorial Sloan Kettering Cancer Center/Evelyn H. Lauder Breast and Imaging Center, New York, NY 10065, USA
- g Department of Radiology, Memorial Sloan Kettering Cancer Center/Evelyn H. Lauder Breast and Imaging Center, New York, NY 10065, USA
- ^h Kavli Institute at Cornell for Nanoscale Science, Cornell University, Ithaca, NY 14853, USA
- i Department of Biomaterials, Max Planck Institute of Colloids and Interfaces, Research Campus Potsdam-Golm, 14424 Potsdam, Germany
- ^j Department of Civil and Environmental Engineering, Massachusetts Institute of Technology, Cambridge, MA 02139, USA

ARTICLE INFO

Keywords: Pathological mineralization Raman microscopy Multimodal imaging Biogenic whitlockite Dystrophic mineralization Label-free nondestructive chemical imaging

ABSTRACT

Microcalcifications (MCs) are routinely used to detect breast cancer in mammography. Little is known, however, about their materials properties and associated organic matrix, or their correlation to breast cancer prognosis. We combine histopathology, Raman microscopy, and electron microscopy to image MCs within snap-frozen human breast tissue and generate micron-scale resolution correlative maps of crystalline phase, trace metals, particle morphology, and organic matrix chemical signatures within high grade ductal carcinoma *in situ* (DCIS) and invasive cancer. We reveal the heterogeneity of mineral-matrix pairings, including punctate apatitic particles ($<2\,\mu\text{m}$) with associated trace elements (e.g., F, Na, and unexpectedly Al) distributed within the necrotic cores of DCIS, and both apatite and spheroidal whitlockite particles in invasive cancer within a matrix containing spectroscopic signatures of collagen, non-collagen proteins, cholesterol, carotenoids, and DNA. Among the three DCIS samples, we identify key similarities in MC morphology and distribution, supporting a dystrophic mineralization pathway. This multimodal methodology lays the groundwork for establishing MC heterogeneity in the context of breast cancer biology, and could dramatically improve current prognostic models.

1. Introduction

Microcalcifications (MCs), small calcium mineral deposits in breast tissue, are detected by mammography and serve as critical diagnostic indicators of non-palpable breast cancer (Wilkinson et al., 2017). MCs are thought to be associated with 80–95% of all ductal carcinoma *in situ* (DCIS) cases, as well as some high risk invasive cancers, with poorer patient prognosis reported in some cases (Ferranti et al., 2000; Tse et al., 2008). The diagnostic relevance of MCs stems from their characteristic mammographic appearances that vary with pathology, from

benign lesions to invasive cancer (Wang et al., 2014). Histopathology indicates that MC morphology differs even within DCIS subtypes, a cancer precursor defined by neoplastic cellular proliferation within one or more mammary duct(s) (Hoda et al., 2014; Holland and Hendriks, 1994; Tse et al., 2008). MCs range from large (>100 μ m) "laminate" masses in low-grade DCIS to distributed "granular" particles in aggressive comedo-type DCIS, a subtype characterized by high grade nuclear features and central necrosis within the mammary duct, as sketched in Fig. 1.

Furthermore, MCs associated with invasive cancers occur in the

E-mail addresses: cf99@cornell.edu (C. Fischbach), masic@mit.edu (A. Masic), lae37@cornell.edu (L.A. Estroff).

Abbreviations: MCs, microcalcifications; DCIS, ductal carcinoma in situ; SHG/IF, second harmonic generation microscopy with intrinsic fluorescence microscopy; NCPs, non-collagenous proteins

^{*} Corresponding authors at: Nancy E. and Peter C. Meinig School of Biomedical Engineering, Cornell University, Ithaca, NY 14853, USA (C. Fischbach). Department of Civil and Environmental Engineering, Massachusetts Institute of Technology, Cambridge, MA 02139, USA (A. Masic). Department of Materials Science and Engineering, Cornell University, Ithaca, NY 14853, USA (L.A. Estroff).

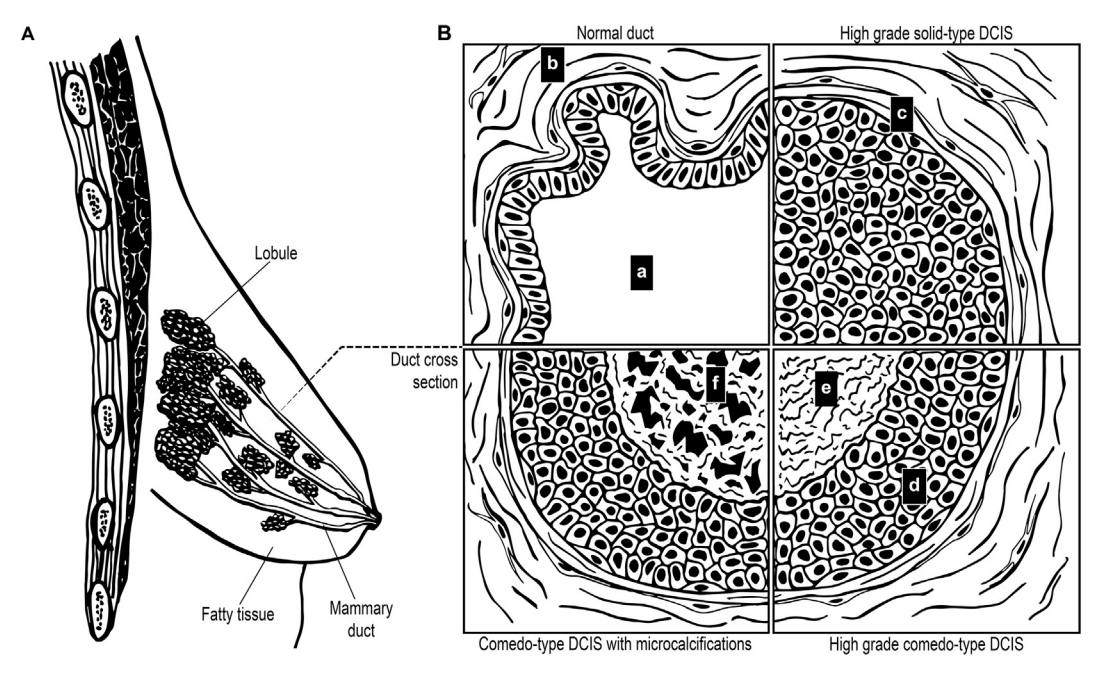


Fig. 1. Schematic of breast tissue and DCIS. (A) Normal breast tissue is comprised of lobules, ducts and supporting soft tissues. The surrounding tissue consists of fat, fibrous connective tissue and a network of blood and lymph vessels (for clarity, not shown). (B) A cross-sectional schematic representing a possible time progression of DCIS (clockwise): a normal duct, high grade solid DCIS, comedo-type DCIS with characteristic central necrosis, and comedo-type DCIS presenting microcalcifications. Structures indicated: lumen (a), stroma (b), basement membrane (c), viable cell zone (d), necrosis (e), and necrosis with calcification (f). Schematics are not to scale.

desmoplastic stroma alongside invasive cancer cells that have breached the ductal membrane (Hoda et al., 2014). A more nuanced understanding of the chemistry of the MCs and associated microenvironment has the potential to expand their diagnostic relevance. Multimodal imaging techniques are used here to obtain correlative maps of local chemical signatures of breast tumor-associated MCs within their native organic matrix.

Like other types of pathological mineralization (Bazin et al., 2012; Bertazzo et al., 2013; Hutcheson et al., 2016; Olafson et al., 2015; Poloni and Ward, 2014; Rimer et al., 2010), the formation of MCs most likely involves complex interactions among system-specific biological moieties (e.g., proteins, extracellular matrix, cells, etc.) and mineral components. As is well-studied in biomineralization (Weiner and Addadi, 2011), these mineral-matrix interactions are responsible for determining the mineral phase and morphology. In breast tissue, MC mineral phase has been linked to pathology: Type I calcium oxalate dihydrate (CaC₂O₄•2H₂O), which are birefringent, bipyramidal crystals and are typically associated with benign breast diseases (Büsing et al., 1981; Radi, 1989), and Type II non-stoichiometric apatite crystals (i.e., (Ca,Na)₁₀(PO₄,CO₃)₆(OH,F)₂), which vary in morphology, including needles, punctate particles, and aggregates, and occur in both benign and malignant breast tumors (Ahmed, 1975; Baker et al., 2010; Frappart et al., 1986; Haka et al., 2002). There are also reports of a third type of MC, whitlockite, also known as magnesium-substituted beta-tricalcium phosphate ((Ca,Mg)₃(PO₄)₂), whose presence was recently correlated with increasing malignancy (Hassler, 1969; Scott et al., 2016). Other studies have looked at compositional variation among apatitic MCs, including elevated magnesium, sodium, and decreased carbonate content in MCs associated with more malignant tumors (Baker et al., 2010; Haka et al., 2002; Scimeca et al., 2014; Scott et al., 2017). Little is known, however, about the mineralization pathways that lead to MC formation, the composition of the biological matrix in which they are formed, the chemical distinctions between MCs associated with benign and malignant tissues, and their relationship to tumor progression.

To date, the majority of research focusing on materials properties of MCs in breast tissue has been performed using either dissected mineral (Büsing et al., 1981; Frappart et al., 1986, 1984; Hassler, 1969) or

otherwise fixed or dehydrated tissue samples (Ahmed, 1975; Baker et al., 2010; Ben Lakhdar et al., 2016; Haka et al., 2002; Poggi et al., 1998; Scimeca et al., 2014; Scott et al., 2017; 2016). These sample preparation techniques can often introduce artifacts and make interpretation of mineral-matrix relationships difficult. The emergence of materials science techniques that do not require extensive sample preparation and can be used correlatively to characterize both the organic and inorganic components of mineralized tissue (Bergholt et al., 2016; Bertazzo et al., 2013; Hendley et al., 2015; Vidavsky et al., 2016, 2014), presents an opportunity to address these questions about MCs within a diagnostically relevant framework. Importantly, spectroscopic imaging techniques that can be performed without damaging the tissue, on unfixed, hydrated samples, have the potential to be coupled with histopathology and electron microscopy (EM) to provide spatially resolved maps of both organic and inorganic chemical signatures, correlated with pathological features. Raman microscopy offers one such promising approach and has been applied to analyze breast tumors previously (Kneipp et al., 2003; Schaeberle et al., 1996; Shafer-Peltier et al., 2002; Surmacki et al., 2013), but none of these studies specifically mapped MCs and their local tissue environments. The combination of histopathology and confocal Raman microscopy, an approach in which sample preparation and instrumentation are feasible in modern pathology labs (Bhargava and Madabhushi, 2016; Cheng and Sie, 2015), has potential to extend diagnostic capabilities well beyond what is currently available.

In this work we used multimodal spectroscopy and imaging to characterize MCs and their associated matrix in human breast cancer tissue sections (Fig. 2, Supplementary Table S1). Readily accessible, snap-frozen tissue was used to ensure that no special tissue preparation techniques were required and that the samples remained unfixed. The in-registry techniques used include confocal Raman microscopy, second harmonic generation microscopy simultaneous with intrinsic fluorescence multiphoton microscopy (SHG/IF), and secondary and back-scattered electron microscopy in conjunction with energy dispersive spectroscopy (SE/BSE/EDS). Additionally, we employed an emerging technique, air-operational scanning electron microscopy (airSEM), which enables backscattered imaging and EDS X-ray mapping of uncoated tissue in air with minimal sample processing (Nguyen et al.,

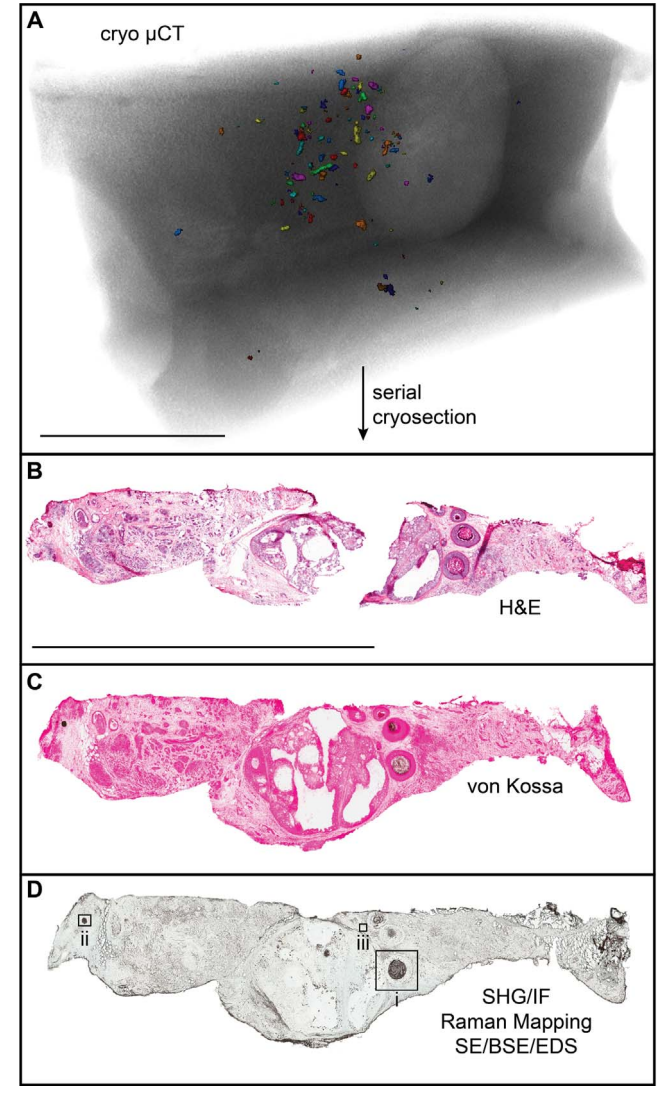


Fig. 2. Experimental design. (A) μ CT 3D rendering of frozen human breast tissue. Calcification clusters are represented in color while tissue and embedding media appear grey. (B–D) Representative serial sections from Sample 1: (B) H&E, (C) von Kossa, and (D) multimodal analysis including SHG/IF, confocal Raman microscopy, and SE/BSE/EDS. ROIs are boxed: Region (i) is high grade comedo-type DCIS with calcification, region (ii) is a stromal calcification associated with benign tissue, and region (iii) is high grade solid-type DCIS with no necrosis or calcification. Scale Bars: 5 mm.

2013, 2016; Solomonov et al., 2014; Vidavsky et al., 2014). Using this multimodal approach, we could correlate the crystal phase, nanoscale particle morphology, trace element content, as well as the chemistry of the associated organic matrix, for spatially localized individual MCs, ranging in size from $>100~\mu m$ to $<2~\mu m$.

2. Materials and methods

2.1. Breast tissue samples

Ductal carcinoma *in situ* samples (DCIS 1, 2, 3 from Samples 1, 2, 3 respectively) and an invasive tumor sample (Sample 4, Supplementary Table S2) were obtained from Memorial Sloan Kettering Cancer Center. Samples were snap frozen in optimal cutting temperature compound (OCT) immediately after surgical removal via mastectomy.

2.2. Cryo-μCT

Tissue blocks were scanned using high resolution X-ray micro-

computed tomography (Zeiss Versa XRM-520). The system set-up contains a rotating sample holder positioned between the X-ray source and detector. The X-rays are produced in a cone beam configuration with a source voltage of 150 kV and a power of 10 W. Calibration standards for bone hydroxyapatite and synthetic oxalate were scanned prior to the tissue. Samples were placed on a cold metal block that was partly submerged in liquid nitrogen, and left to equilibrate for 30 min prior to imaging. Samples were scanned with 1601 projections over 192 degrees, with a resolution of $20\,\mu\text{m/pixel}$ and the detector was binned such that projections were 1000×1000 pixels in size. Data was scaled using the calibration standards in the Xradia software.

2.3. 3D µCT image generation

Analysis of the μ CT data was carried out on the image stack using Avizo® Fire to visualize the calcifications within the tissue in 3D. The data set was cropped and calcifications were then segmented from the surrounding tissue/embedding media using a thresholding technique based on the difference in density between the calcifications and tissue/embedding media. The volume rendered 3D model was made from the segmented data sets for the calcifications and tissue block.

2.4. Sample sectioning

Samples were sectioned on a microtome (Thermo Scientific HM550 Cryostat). Four serial sections were cut from each sample: two $12\,\mu m$ -thick sections mounted (Fisherbrand® Superfrost®/Plus microscope slides) for histological analysis, using hematoxylin and eosin (H&E) and von Kossa/Nuclear Fast Red respectively, and one thicker section (20 μm) mounted on a fused quartz slide (Electron Microscopy Sciences) for multimodal analyses (SHG/IF, Raman, airSEM/SEM/EDS). Histological sections were baked at 65 °C for 45 min to adhere the sample to the slide, and were processed at the Cornell College of Veterinary Medicine Animal Health Diagnostic Center using standard protocols for the stains. The thicker section was not baked (to preserve structure).

All sections (histology and unstained) were imaged using a Scanscope® CSO (Aperio, Vista, CA) at $40\times$ magnification. Stained sections were then reviewed carefully to select regions of interest based on the von Kossa staining. Pathological grading was assessed using the H&E stained sections. The white light image of the thick section provided landmarks to guide proper registry of regions of interest (ROIs) during all other analysis techniques.

2.5. Second harmonic generation and multiphoton intrinsic fluorescence microscopy imaging

SHG/IF and Raman were carried out using immersion objectives with phosphate buffer-hydrated tissue to avoid conformational changes in the tissue, to be consistent between techniques, to minimize damage, and to mimic physiological conditions to the best of our abilities. Additionally, for SHG/IF, two-photon-excited fluorescence limits damage as the excitation source is in the infrared (Zipfel et al., 2003).

Multiphoton and second harmonic generation microscopies were carried out on an in-house system consisting of a femtosecond pulsed Ti:Sapphire laser excitation source ($<\!100$ fsec output pulses at 80 MHz, Mai Tai HP, Spectra-Physics, Mountain View, CA) centered at 780 nm. Laser light was circularly polarized using a Berek variable waveplate (5540, New Focus, San Jose, CA) placed before the scanner to prevent orientational dependencies in the resultant images. Samples were hydrated in DPBS (Dulbecco's Phosphate Buffered Saline; KCl: 2.67 mM, KH₂PO₄: 1.47 mM, NaCl: 136.9 mM, Na₂HPO₄: 8.1 mM) and imaged through a 20×, 0.95 NA water immersion objective (Olympus XLUMPlanFl) on an Olympus BX61WI microscope interfaced to a BioRad 1024 scanner and acquisition system. Images were simultaneously collected in two channels: 320–380 nm (for SHG signal) and

410–490 nm (for intrinsic fluorescence signal) using non-descanned Hamamatsu (Bridgewater, NJ) bialkali photomultiplier tubes with signals amplified and integrated into the BioRad electronics. See Supplementary material for SHG/IF image processing.

2.6. Dehydration and rehydration

Following SHG analysis samples were removed from DPBS and dehydrated in an ethanol series (25, 50, 70, 95, 100% ethanol, 5 min in each) for storage and transport. They were rehydrated prior to Raman imaging using the same series in reverse. This step is thought to remove certain components of breast tissue (i.e., fat) but was not considered harmful to the collagen, cells, other proteins, or microcalcifications. Samples containing regions where microcalcifications were detected using Raman or airSEM underwent an additional dehydration/rehydration step to verify the continued presence and unaltered appearance of the microcalcifications. DCIS regions were noted to lose organic material through repeated dehydration/rehydration, so we attempted to minimize this step as much as possible.

2.7. Raman imaging and data analysis

A confocal Raman microscope (alpha300RA, WITec, Ulm, Germany) with a frequency doubled Nd:YAG laser (532 nm) excitation source was used. The CCD detector (DU401A-BV, Andor, UK) was placed behind the spectrometer (UHTS 300; WITec) with a grating of 600 g/mm (BLZ = 500 nm). Samples were placed on the stage (piezoscanner), immersed in phosphate buffer solution (DPBS) and imaged using a water immersion $60\times$ objective (Nikon, NA = 1.0). The lateral resolution was around 0.61 λ /NA. The mapping scanning stepsize used was 1 μ m with an integration time of 0.4–0.5 s per step.

Data were analyzed using WITec Project Plus (Versions 2.10 and 4.1) including peak integration heat maps and combination image formation (Supplementary Fig. S5). Averaged subtraction spectra as depicted in Supplementary Fig. S4 were carried out manually (Supplementary material).

2.8. Air scanning electron microscopy and energy dispersive X-ray spectroscopy

AirSEM (B-nano Ltd.), was used to image uncoated dry samples to examine calcification shape and morphology. EDS was used to determine the elemental composition. ROIs were located using the built-in "in-registry" optical microscope and then shuttled to the airSEM, consisting of an upright configuration (standard Mira Tescan column) with chambers under high vacuum that enable generation, focusing, and scanning of the primary electron beam (Schottky field emitter) and house the in-beam backscattered electron detector (B-nano) and EDS Xray detector (Bruker, XFlash 6). A thin (5-20 nm thick) electron transparent window (silicon nitride, TEMwindows.com, SiMPore Inc., Rochester NY) separates the vacuum chamber from the sample allowing imaging in an air-helium mixture with a distance from the window of approximately 50 µm. Imaging and elemental maps were carried out from 10 to 15 keV with a beam current 1000–1500 pA. Elemental maps were acquired for at least 5 min. The Esprit EDS software used to generate maps and analyze EDS data.

2.9. Standard scanning electron microscopy in conjunction with EDS

After all analysis was complete SEM/EDS was used to verify the morphological and elemental findings and to take higher resolution images of calcifications. Samples were carbon coated ($\sim 15\,\mathrm{nm}$ thick) and analyzed in a Mira3 FESEM (Tescan, Czech Republic). High resolution images were acquired at $5\,\mathrm{keV}$ (working distance $3\,\mathrm{mm}$) with the in-beam secondary electron detector and/or the in-beam back-scattered electron detector. EDS was carried out at $20\,\mathrm{keV}$ (working

distance 15 mm) using the EDS detector (Bruker). EDS maps were acquired for at least 5 min and a minimum of 4 particles were examined from each DCIS region. The Esprit EDS software was used to generate maps and analyze EDS data.

3. Results

3.1. Histopathology

Snap-frozen human breast tumor samples were selected for serial sectioning based on histopathologic identification of high grade DCIS or invasive carcinoma with associated MCs (see Supplementary Table S2 for patient information). We selected three high grade comedo-type DCIS cases, one invasive cancer, and one benign stromal calcification. A representative progression of sample processing and analysis is shown for Sample 1 in Fig. 2. High resolution cryo-X-ray micro-computed tomography (µCT) was used to visualize the distribution and extent of calcifications within the tissue (Fig. 2A). Samples were cryosectioned to obtain three adjacent sections. Regions of interest (ROIs) were identified in the first two sections using standard histopathologic stains: hematoxylin and eosin (H&E), the basis of pathological assessment, and von Kossa, to locate phosphate-containing minerals (Fig. 2B and C). Samples 1, 2, and 3 contained at least one duct presenting high grade comedo-type DCIS with the characteristic central necrosis that also stained brown in von Kossa (Fig. 2D, Box (i), Supplementary Figs. S1 and S2 respectively). For Sample 1, another duct presenting high grade solid-type DCIS without von Kossa staining served as a comparison region (Fig. 2D, Box (iii)). Additionally, an ROI from Sample 1 was analyzed that stained brown in von Kossa, but was not associated with epithelial cells and was pathologically determined to be benign tissue (Fig. 2D, Box (ii)). We refer to this as a stromal calcification. Sample 4 had extensive invasive carcinoma confirmed with H&E and MCs were identified with von Kossa (Supplementary Fig. S3).

3.2. Non-destructive multimodal characterization of microcalcifications and surrounding matrix

Both SHG/IF and confocal Raman microscopy were performed on the same hydrated tissue sections (Fig. 3). To illustrate the correlative capabilities of these two non-destructive techniques, we focused on two distinct MC-containing ROIs in Sample 1 and comparable ROIs that were mineral free: high grade DCIS without necrosis (Fig. 3A–D), high grade DCIS with necrosis (Fig. 3E–H), stroma (Fig. 3I–L), and a stromal calcification (Fig. 3M–P).

3.2.1. DCIS without central necrosis

The duct presenting high-grade solid-type DCIS without central necrosis shows no von Kossa staining, indicating a lack of phosphate mineral (Fig. 3A and B). The SHG signal from crystalline fibrillar collagen maps to the pink-stained stroma tissue surrounding the duct in the serial H&E section image (Fig. 3C). Using confocal Raman microscopy, several different spectral signatures were identified based upon characteristic bands: collagen, DNA-like, and "non-collagenous proteins" (NCPs) (see Supplementary Text for details of spectral analysis). For this study, we grouped all proteins, excluding collagen, into an average spectral signature that we refer to as NCPs, not to be confused with bone-specific NCPs (Boskey, 1989). The Raman combination map shows collagen surrounding the duct, spatially correlating with the SHG collagen signal (Fig. 3D, Supplementary Figs. S4 and S5). Within the duct, DNA-like signatures are seen with demonstrably large and irregular cell nuclei, matching approximately the size of the purple-stained nuclei in the H&E image, surrounded by NCPs. Outside the duct, smaller concentrations of DNA-like signatures, consistent with the presence of elongated nuclei of stromal cells including fibroblasts, are present along the collagen. Significantly, in agreement with the von Kossa stain, no apatitic Raman spectral signatures were detected either

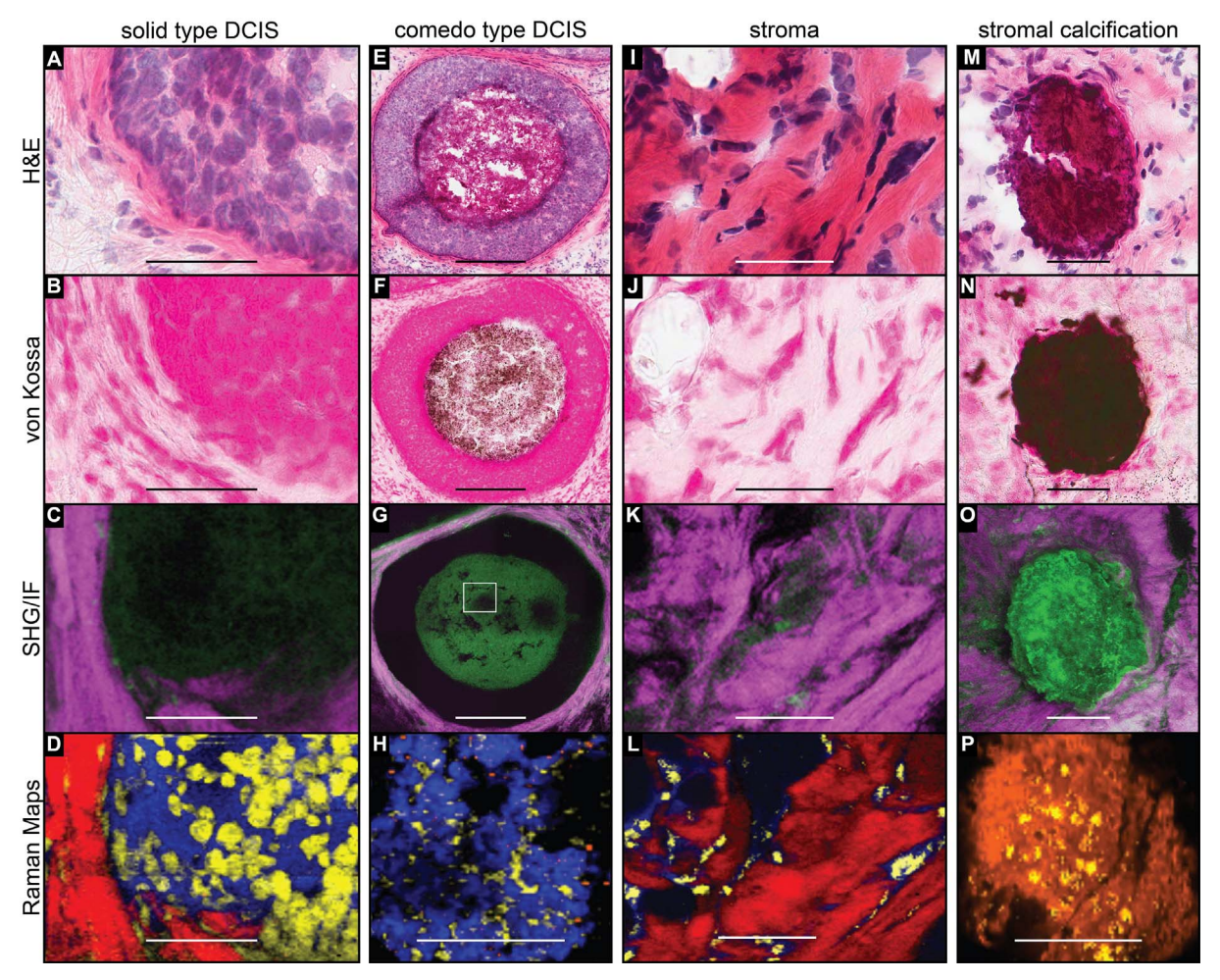


Fig. 3. Nondestructive multimodal characterization of MCs and matrix. (A–D) High grade solid-type DCIS with neither necrosis nor calcification, (E–H) high grade comedo-type DCIS with necrosis and calcification, (I–L) stroma and (M–P) stromal calcification associated with benign tissue. H&E and von Kossa staining images were taken from serial sections. SHG/IF (magenta/green) images and confocal Raman microscopy combination maps (Supplementary Fig. S5, Supplementary Table S3) were acquired hydrated on the same section. Raman combination maps show overlaid false color heat maps of collagen (red), NCPs (blue), DNA-like (yellow), and apatite (orange). Proteins have been excluded from (P) for clarity. The white box in (G) indicates the location of Raman sampling in (H). Scale Bars: (E–G): 200 μm, All others: 50 μm.

within or surrounding the duct.

3.2.2. DCIS with central necrosis

A second duct was pathologically determined to be high grade comedo-type DCIS with characteristic central necrosis surrounded by a region of viable neoplastic cells (Fig. 3E). While the viable cell zone appears pink in the von Kossa image, the central necrotic area of the duct stained brown, which suggests the presence of calcium phosphate mineral (Fig. 3F). The SHG image shows fibrillar collagen surrounding the duct similar to the non-necrotic duct, with no fibrillar collagen evident within the duct (Fig. 3G). The IF signal within the necrotic zone of the duct appears stronger and more homogenous than either in the non-necrotic duct or in the neighboring viable cell region (Gupta and Majumder, 1997).

A Raman combination map of NCPs, DNA-like, and apatitic spectral signatures was generated (Fig. 3H). Collagen spectral signatures were not observed, affirming results from SHG. The majority of the area contained NCPs with DNA-like signatures dispersed throughout in a fragmented and unorganized manner, a key observation that cannot be made with standard histochemical analysis. Importantly, in contrast to the non-necrotic duct, small mineral particles ($<2\,\mu\text{m}$), with a primary Raman band at 961 cm $^{-1}$ (consistent with apatitic phosphate), were detected within the necrosis. The Raman map of DCIS 3, from another patient had similar $<2\,\mu\text{m}$ particles with a clear apatite signature dispersed within a matrix of NCPs, as well as areas of mixed cholesterol-

like/carotenoid signature (Supplementary Fig. S2d). In comparison to DCIS 1, no DNA-like spectral signature was detected within the necrotic core. The composition of the organic matrix in both DCIS 1 and 3 is consistent with cellular material and/or debris, as expected for necrotic tissue.

3.2.3. Stroma

Fibrillar collagen is the primary component of the representative dense stromal region shown (Fig. 3I). There was no staining in von Kossa (Fig. 3J) and SHG and Raman signals for collagen are spatially correlated (Fig. 3K and L). Unknown endogenous fluorophores can also be seen using IF (Zipfel et al., 2003). Raman revealed NCPs localized around DNA-like signatures, in contrast to the cancerous ducts, where the DNA-like signatures (i.e., cell nuclei) appear densely amidst an abundance of NCPs (Fig. 3L and D).

3.2.4. Stromal calcification

The calcification shown in Fig. 3M was pathologically determined to be of unknown origin, but associated with benign tissue. It stained darkly in von Kossa (Fig. 3N), presenting as a dense mass. The SHG image reveals crystalline collagen in direct contact with the surface of the calcification but not inside of it (Fig. 3O, Supplementary Fig. S6a and b). The calcification also had a strong IF signal, which could originate either from endogenous fluorophores within the calcification or from the mineral itself (Waychunas, 2002). From Raman mapping, the

mass was identified as apatite, with interspersed regions of DNA-like material and NCPs, surrounded by collagen (Fig. 3P, Supplementary Fig. S6c and d).

The stromal MC is a dense aggregate of apatite ($\sim 100\,\mu m$ in diameter), encapsulated by collagen (Fig. 3O, Supplementary Fig. S6a–c). The intimate association with collagen, coupled with the DNA signatures present within the MC, strongly suggests either an active secretory process, whereby mineral is forming around intact cells, or possibly a foreign body response in which the calcification is wrapped in collagen to isolate it from the surrounding tissue. Though we could not confirm the presence of live cells or intact nuclei from the serial H&E stain (due to the dominating stain of the mineral itself) the morphologically relevant clusters of DNA-like signatures in the Raman heat map present a noteworthy contrast to the fragmented DNA-like signatures from the necrotic region in DCIS 1. Finally, the co-localization of protein signatures with the apatite signature throughout the stromal MC, suggests that the mineral contains proteinous inclusions (Supplementary Fig. S6d) (Haka et al., 2002).

3.3. Distribution and morphology of DCIS MCs

We used SEM in both secondary electron (SE) and back-scattered electron (BSE) modes to image the distribution and morphology of particles within high grade comedo-type DCIS from 3 different patients (DCIS 1, 2, and 3) as well as the stromal calcification from Sample 1 (Fig. 4, Supplementary Fig. S6).

BSE imaging, where brighter contrast indicates higher mineral content, of the necrotic cores of all three DCIS samples shows particles ranging in size from <100 nm, well below mammographic or histopathological detection, to larger individual punctate MCs (spanning a range of sizes but typically <2 µm) broadly distributed throughout the necrotic region (Fig. 4A–C, Supplementary Fig. S2g and h). For DCIS 1 (Fig. 4A) and DCIS 3 (Fig. 4C) the MCs appeared more distinct from the surrounding nanoparticles, whereas for DCIS 2 (Fig. 4B) there were also large regions of dense coverage where individual MCs could not be discerned. For all DCIS samples, no bright particles or areas were observed by BSE amidst the collagen encircling the ducts or within the viable cell zones surrounding the necrotic cores. MCs from all samples appeared closely associated with the organic matrix, in particular, MCs from DCIS 2 and DCIS 3 often appeared indistinguishable from the matrix without the use of BSE imaging (Supplementary Fig. S2g and h).

To further inspect the morphology, individual MCs from DCIS samples were imaged using secondary electrons (SE) revealing MC shape and texture. Aggregate morphologies, in which MCs consist of smaller subunits ($\sim 50 \, \mathrm{nm}$) were found in all three DCIS samples (Fig. 4, insets). This texture was particularly well-pronounced among MCs throughout the calcified region of DCIS 1. Interestingly, at higher magnification, the stromal calcification also appeared to be composed of aggregated nanoparticles of similar sizes (Supplementary Fig. S6e–h). Many of the MCs in DCIS 1 were ovoid in shape (Fig. 4A inset),

while particles in DCIS 2 and DCIS 3 had more haphazard aggregate subunits and aggregate MC shapes were extremely varied (Fig. 4B and C insets). Similar aggregate surface morphologies with subunits ranging from 20 to 50 nm have been reported for a range of biominerals (Addadi et al., 2006; Gal et al., 2014; Hovden et al., 2015), and are suggested to be related to formation via particle-accretion, possibly of amorphous nanoparticles that subsequently crystallize (De Yoreo et al., 2015; Gal et al., 2015).

3.4. Comparative analysis of phase and composition of microcalcifications across DCIS samples

To explore in detail the crystalline phase and trace-element composition of the MCs in the different samples, we used Raman spectroscopy and EDS, respectively (Fig. 5). From the same Raman data sets used to create the combination maps (Fig. 3H, P, Supplementary Fig. S2d), average Raman spectra for apatitic MCs were calculated (Fig. 5A, see Supplementary Text for details regarding average spectra generation). The spectra of DCIS 3 and the stromal calcification are characteristic of B-type carbonate substituted apatite (Cuscó et al., 1998; Penel et al., 1998). Though the DCIS 1 spectrum is averaged over a small number of spectra, the prominent peak at 961 cm⁻¹ is suggestive of apatite. A higher resolution combination map of this area reveals an individual apatitic MC in close proximity to NCPs and potentially in intimate contact with DNA-like compounds (Fig. 5A, inset). A raw spectrum from an MC pixel is shown and is consistent with an apatitic phase.

Average EDS spectra for the three DCIS samples and the stromal calcification, with their acquisition regions displayed in the corresponding BSE images, are shown in Fig. 5B. The identification of apatite in DCIS 1 and 3 by Raman is corroborated by the prominent presence of calcium and phosphorus peaks in the EDS spectra. Although the Raman mapping data acquired for DCIS 2 was in the viable cell zone (Supplementary Fig. S1d), the average EDS spectrum acquired in the necrotic region bears a striking resemblance to that of DCIS 1. Additional trace elements are detected for all the calcifications in varying proportions: sodium and aluminum are particularly prominent for particles in DCIS 1 and DCIS 2 while fluorine was unique to particles from DCIS 3. The stromal calcification has trace amounts of iron, nickel and zinc with a notable lack of contribution from sulfur. Due to the particle sizes and rough surfaces, quantitative analysis was not feasible, but elemental profiles were consistent among particles originating from the same duct, even those spatially separated by hundreds of microns.

Representative individual EDS elemental maps are shown in Fig. 5C along with a corresponding high resolution secondary electron image acquired for the MC encircled in (Fig. 5A, inset) and (Fig. 5B, d). Sodium and aluminum signals spatially coincide with calcium and phosphorus, whereas silicon (originating from the quartz substrate) does not. Sulfur appears ubiquitously on the EDS map so it is not exclusively associated with the MCs. These findings were confirmed using EDS in

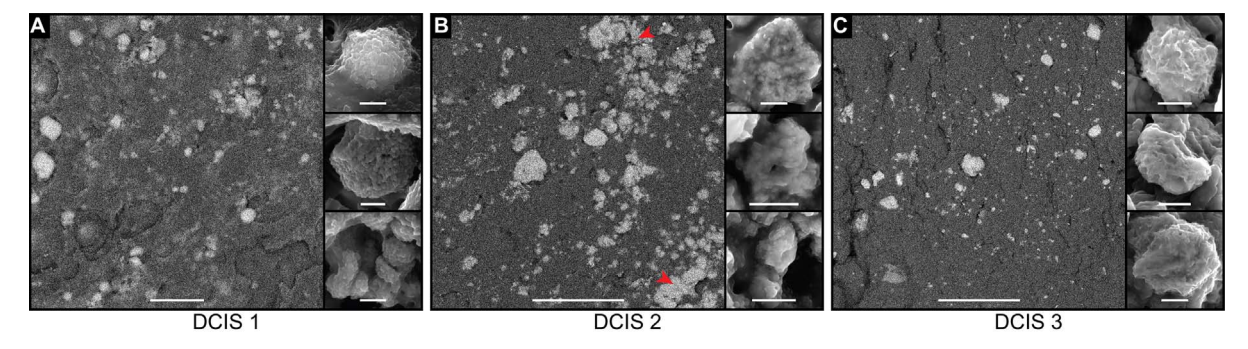


Fig. 4. DCIS nanoparticle distribution and morphology. BSE images of three representative regions from the necrotic cores of each high grade DCIS: DCIS 1 (A), DCIS 2 (B), and DCIS 3 (C). SE images of representative particle morphologies from each region are shown to the right of the large BSE images. Red arrowheads indicate regions of dense mineral in (B). Scale bars: BSE: 5 µm; SE: 500 nm.

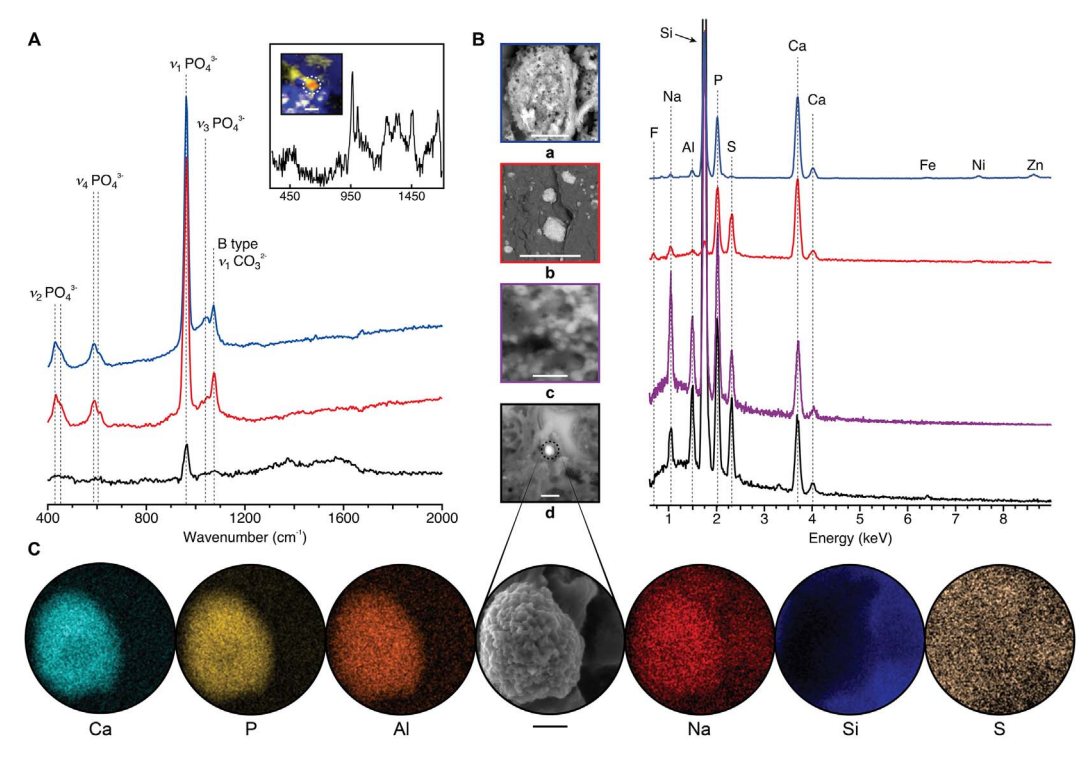


Fig. 5. Spectroscopic Analysis. (A) Raman average subtraction spectra for the stromal calcification (Fig. 3P), DCIS 3 MCs (Supplementary Fig. S2d), and DCIS 1 MCs (Fig. 3H) are shown as blue, red, and black traces. Vibrational modes for B-type carbonated apatite are indicated: v1 (symmetric P—O stretch), v3 (asymmetric P—O stretch), v2 and v4 (O—P—O bending), and carbonate v1 (symmetric C—O stretch). The inset is a raw spectrum from the apatitic MC encircled in the Raman combination map inset (apatite: orange; NCPs: blue; DNA-like: yellow). (B) Average EDS spectra, normalized to the calcium peak are shown with their BSE acquisition regions: stromal calcification (blue, a), DCIS 3 (red, b), DCIS 2 (purple, c), and the MC encircled in (A) from DCIS 1 (black, d). The silicon peak originates from the quartz substrate. (C) Individual EDS elemental maps and the corresponding SE image (center) were acquired for the MC encircled in (A, inset) and (B, d). Images and spectra in (a), (c), and (d) were acquired using airSEM while (b) and (C) were acquired using SEM. Scale Bars: (A, inset) 3 μm, (B, (a)) 30 μm, (B, (b–d)) 3 μm, (C) 500 nm.

conjunction with both airSEM (Fig. 5B, black curve) and traditional SEM on the same particle as well as others (Fig. 5C center; Supplementary Fig. S7). EDS spectra of two control regions, a high grade DCIS with light von Kossa staining and a stromal region, were also acquired (Supplementary Fig. S8). In both regions there were no obvious brightly backscattering regions, which would have indicated possible mineral particles. The corresponding EDS spectra were consistent with organic material mounted on a quartz slide.

The presence and spatial localization of trace element signatures was consistent across all DCIS MCs analyzed in both DCIS 1 and DCIS 2 (Supplementary Figs. S1g and S7). DCIS 3 differs in trace element composition, with the presence of fluorine and much smaller contributions from sodium and aluminum, all concomitant in EDS mapping (Supplementary Fig. S2k). Both sodium and fluorine are well-studied apatite substituents (Fleet, 2013). Aluminum substitution, as seen in DCIS 1 and 2, has been less studied, but has been observed in synthetic apatites (Tanizawa et al., 1990) and found in bone (Chappard et al., 2016). Previous studies have reported the possibility of aluminum in MCs, though none have spatial maps to localize the Al to the MCs (Frappart et al., 1986; Galkin et al., 1982). Interestingly, aluminum has been reported in significantly higher levels in cancerous breast tissue (Ng et al., 1997) and nipple aspirate fluid from breast cancer patients (Mannello et al., 2013). Our results, coupled with another recent report regarding trace elements in MCs (Scott et al., 2017), provide a clear imperative to further study the relationship between trace element composition of MCs and breast cancer malignancy.

3.5. Multimodal characterization of invasive MCs

Using the multimodal characterization methodology developed here, we analyzed a region of invasive carcinoma with associated MCs (Fig. 6). H&E reveals clustered invasive cancer cells in a collagen-rich

region, often with cytoplasms demarcated by large swathes of collagen (Fig. 6A, left). MCs are evident in von Kossa staining (Fig. 6A, right). There are two distinctive appearances: a large mass and a smattering of particulates (Fig. 6A, upper and lower box respectively). Raman reveals that these are actually two different phosphate-mineral phases, indistinguishable by histology: apatite and whitlockite (Fig. 6F).

3.5.1. Invasive apatite MC

The Raman combination map for the upper region shows a large apatite mass amidst collagen and cell clusters with some cholesterol-like components nearby (Fig. 6B). SE images of the same MC show a large mineral aggregate encased in organic matrix, which limits BSE visualization under these acquisition parameters (Fig. 6C and D). Close inspection of exposed mineral reveals possible subunits (Fig. 6E). The average subtraction spectrum of the orange pixels is consistent with apatite, and so is the elemental composition (Fig. 6F and G). Though the surrounding matrix is collagenous, on subtraction, the protein signature within the apatite-containing pixels from Raman is NCPs and no evidence of mineralized collagen was found using Raman or SE/BSE (Supplementary Fig. S4 – subtraction of apatite from the apatite-containing pixels).

3.5.2. Invasive whitlockite MC

The confocal Raman combination map of the lower region shows whitlockite within a collagenous matrix. Cellular signatures are nearby in addition to cholesterol-like and carotenoid contributions (Fig. 6H). The average subtraction spectrum of the cyan pixels is consistent with whitlockite rather than apatite, showing broader bending modes, and an asymmetric υ_1 phosphate band around 970 cm⁻¹ (Fig. 6F). The representative EDS spectrum shows peaks corresponding to magnesium as well as sodium, aluminum, sulfur, and fluorine (Fig. 6G). SE images taken in the region reveal spheroidal particles (Fig. 6I). A few particles

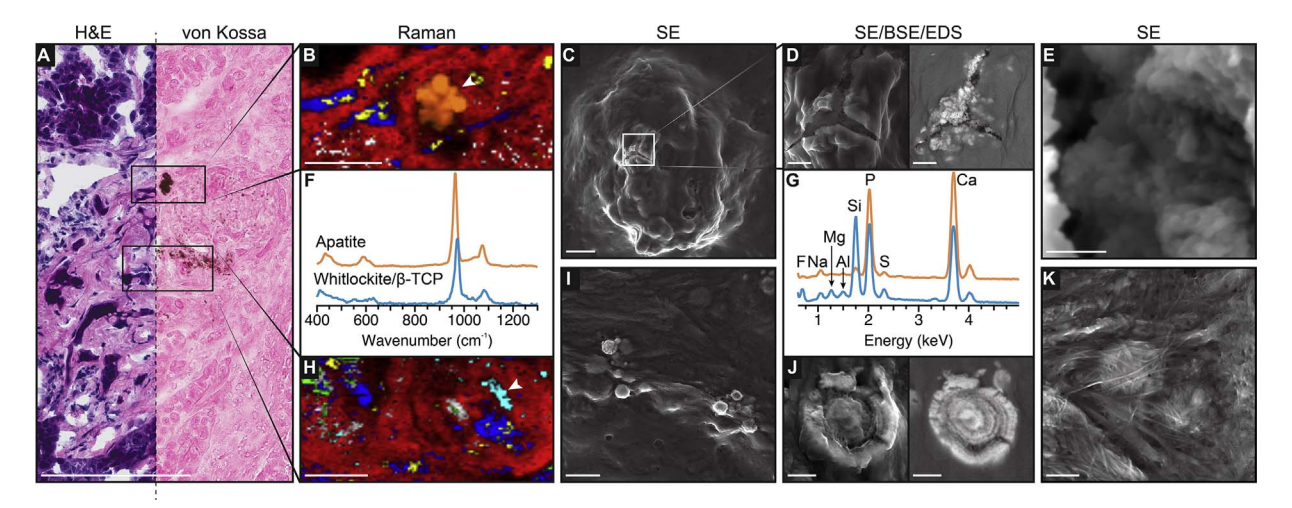


Fig. 6. Invasive cancer MC multimodal analysis. (A) H&E (left) and von Kossa (right) serial sections are shown aligned. Two distinctive MC regions are boxed: a large mass (upper, (B–E)) and a region of granular MCs (lower, (H–K)). (B) Raman combination map corresponding to the upper region (apatite: orange; collagen: red; NCPs: blue; DNA-like: yellow; cholesterol-like: white). (C) SE image of the upper MC (B, white arrow). (D) SE (left) and BSE (right) images from region indicated (C, white box). (E) High magnification SE image of the mineral texture. (F) The average subtraction spectrum (orange) of the orange pixels from (B) is apatitic and so is the average EDS spectrum (G, orange trace). (H) Raman combination map of the lower region (whitlockite: cyan; collagen: red; NCPs: blue; DNA-like: yellow; cholesterol-like: white; carotenoid: green). The average subtraction spectrum of the cyan pixels (F, cyan) is consistent with whitlockite as is the EDS spectrum (G, cyan). (I) SE images taken in the region indicated (H, white arrow) reveal spherical particles and an example of deposition rings evident in SE and BSE (J, left and right). (K) collagen fibrils are evident atop some MCs. Scale Bars: (A) 200 μm, (B) 30 μm, (C) 5 μm, (D) 1 μm, (E) 200 nm, (H) 30 μm, (I) 3 μm, (J) 500 nm, (K) 1 μm.

showed deposition rings evident in SE and BSE (Fig. 6J, left and right). Others were completely covered by collagen fibrils (Fig. 6K). Further SE images show that most particles were generally spheroidal, occurred in clusters and had an apparent aggregate morphology with subunits on the scale of 50 nm (Supplementary Fig. S9). BSE of the entire region shows that, unlike the DCIS apatitic MCs, the whitlockite MCs were clearly localized and not homogenous in distribution (Supplementary Fig. S9). Furthermore, though particles were often associated with collagen, BSE shows that their spheroidal shape was maintained and did not appear to extend along the collagen fibers.

Whitlockite has a history of involvement in pathological conditions, notably bone, cartilage, and aortic media (Lagier and Baud, 2003). A recent report used synchrotron X-ray diffraction to identify a relationship between whitlockite content and breast cancer malignancy, but did not characterize the associated matrix (Scott et al., 2016). The whitlockite MCs analyzed here were found to be spheroids, integrated within a collagenous matrix, and localized along large collagenous tissue features, in stark contrast to the homogenous distribution of DCIS MCs. In addition to calcium, phosphorus, and magnesium, signatures of aluminum, sodium, and fluorine were found concomitantly with the particles. This observation further highlights the need to investigate the origins and implications of unusual trace elements such as aluminum in a variety of MCs. Understanding the link between tumor malignancy and whitlockite requires further investigation, but it may reveal new insights into why whitlockite, rather than apatite, forms in some pathological conditions (Lagier and Baud, 2003).

4. Discussion

In biomineralization, it is well-accepted that mineral-matrix relationships provide key insights into formation mechanisms of the inorganic crystals. In this work, we were able to identify multiple subtypes of MCs within breast tissue by applying a multimodal imaging approach that produced Raman spectroscopic maps correlated with high-resolution electron microscope images and EDS elemental information. This approach enabled us to describe heterogeneity among MCs that could not be seen by histology, including differences in mineral phase, morphology, trace element composition, and cellular and proteinous signatures. Although we focus on a small number of samples, we have generated information-rich multimodal vignettes of both

high-grade DCIS and invasive cancer MCs. Specifically, we characterized three subtypes of apatitic MCs: 1) a large stromal calcification $(>100 \, \mu m)$ encased by fibrillar collagen and in close association with cellular signatures; 2) punctate particles (<2 µm) distributed within a matrix of NCPs and DNA-like signatures, associated with the necrotic cores of DCIS; and 3) an apatite aggregate (10's of µm), associated with invasive cancer, in a matrix containing collagen, cholesterol-like signatures, and NCPs. In addition to apatite, within the invasive cancer, we identify spheroidal whitlockite particles embedded in a fibrillar collagenous matrix containing NCPs, DNA-like, cholesterol-like and carotenoid chemical signatures. Trace element analysis of both apatite and whitlockite MCs via EDS detected the presence of aluminum, which raises interesting questions regarding the origins and implications of such metals within the tumor. This heterogeneity of mineral/matrix pairs within even our limited sample size (4 patients) is consistent with the increasing evidence for heterogeneity among breast cancers (Koboldt et al., 2012), and highlights the need to elaborate the link between MCs and pathology. Finally, the materials characterization of the mineral-matrix pairs gathered from this work will be useful for defining design parameters for in vitro model systems to begin to assess links between mineral properties and cancer cell behavior (Choi et al., 2015; Pathi et al., 2011).

The observed mineral-matrix interactions also provide hints as to the mineralization pathway(s) by which the MCs formed (De Yoreo et al., 2015; Gal et al., 2015; Weiner and Addadi, 2011). Based upon our data, we suggest that while there are multiple mineralization pathways at play, none of the MCs observed in the DCIS and invasive cancer samples analyzed here are osteogenic in origin. Specifically, we identified multiple key similarities in the mineral-matrix relationships among the three high grade comedo-type DCIS samples. The small particle sizes (<2 µm), aggregate appearance, homogeneous distribution, and associated matrix of cellular debris are indicative of a common mineralization pathway involving either precipitation out of a common solution (Frappart et al., 1984) or a regular progression of cell death with associated mineral formation as the necrotic region expands from the center outwards. Either of these scenarios is consistent with a dystrophic or necrosis-based mineralization pathway (Kim, 1995), in agreement with the long-held views of the pathology community regarding the origins of MCs (Ahmed, 1975; Hoda et al., 2014). Significantly for all three DCIS samples, the recently proposed osteogenic

pathway (Cox and Morgan, 2013; Scimeca et al., 2014; Sharma et al., 2016), which would imply mineral deposition by cells in an osteoid matrix composed primarily of fibrillar collagen (Chen et al., 2015; Mohler et al., 2001), is highly unlikely due to the conspicuous lack of collagen associated with the MCs. Since Raman does not provide further identification of specific proteins within the necrotic cores or living cell zones, however, we cannot rule out the possibility of cellular upregulation of proteins commonly associated with bone (Cox and Morgan, 2013; Scimeca et al., 2014). Continued evaluation of a larger sample number of MCs and their associated matrix within DCIS tumors using the combination of spectroscopic and imaging techniques used in this work promises to provide the key to further elucidating the mineralization pathway(s).

The current study highlights the power of multimodal imaging to generate correlative maps of the chemistry and morphology of pathological mineral deposits and their associated matrix, with sub-micron resolution. Digital pathology is emerging as a powerful tool to aid in the diagnosis of a wide range of diseases (Bhargava and Madabhushi, 2016). With the advent of computational algorithms for image correlation and analysis, the ability to integrate data from multiple imaging modalities becomes increasingly possible within standard clinical histopathological practice. Confocal Raman microscopy provides a labelfree sub-micron chemical imaging method that is potentially a key component in such diagnostic toolboxes. As demonstrated here, Raman microscopy can be used to spatially localize multiple chemical signatures (e.g., 6 distinct chemical signatures are shown in Fig. 6H) including organic matrix components and minerals, without the need to visit a synchrotron, dissect out the mineral, or render the tissue unusable for further analysis. The measurements are performed on hydrated, unstained sections, meaning the tissue sections can be further analyzed using a range of techniques, such as electron microscopy. Specific knowledge of chemical signatures associated with malignant tissues gained from this work pave the way for more accurate diagnostic strategies. Furthermore, ex vivo studies, which help us begin to differentiate MC types and mineralization pathways, have the potential to inform the discrimination of cancer subtypes. In particular, understanding the progression of DCIS to invasive cancer (Esserman and Yau, 2015) and characterizing intra-tumor heterogeneity (Marusyk et al., 2012) could benefit from multimodal analytical approaches that spectroscopically and morphologically contextualize the mineral and organic components simultaneously. For all of these reasons, multimodal imaging could be the ideal tool to quantitatively capture the diversity of MCs present in breast cancer, and to advance our ability to assess patient prognosis based on detailed mineral-matrix characteristics.

Acknowledgements

Thanks to Dr. Rebecca Williams for assistance with SHG, the Cornell University Histology Laboratory staff, Section of Anatomic Pathology, Department of Biomedical Sciences and to the Schaffer-Nishimura lab for use of the cryotome. The authors also wish to extend a thanks to Dr. Sunish Mohanan, Dr. Andrew Miller, and Dr. Nora Springer for histopathological assistance.

Funding

Research reported in this publication was supported by the National Cancer Institute of the National Institutes of Health under award number R01CA173083. The content is solely the responsibility of the authors and does not necessarily represent the official views of the National Institutes of Health. This work made use of the Cornell Center for Materials Research Shared Facilities which are supported through the NSF MRSEC program (DMR-1719875), and also supports KXN. Additional imaging data was acquired through the Cornell University Biotechnology Resource Center, with NIH 1S10OD012287 funding.

Conflict of interest

None.

Appendix A. Supplementary data

Supplementary data associated with this article can be found, in the online version, at http://dx.doi.org/10.1016/j.jsb.2017.12.002.

References

- Addadi, L., Joester, D., Nudelman, F., Weiner, S., 2006. Mollusk shell formation: a source of new concepts for understanding biomineralization processes. Chem. Eur. J. 12, 980–987, http://dx.doi.org/10.1002/chem.200500980.
- Ahmed, A., 1975. Calcification in human breast carcinomas: ultrastructural observations. J. Pathol. 117, 247–251. http://dx.doi.org/10.1002/path.1711170407.
- Baker, R., Rogers, K.D., Shepherd, N., Stone, N., 2010. New relationships between breast microcalcifications and cancer. Br. J. Cancer 103, 1034–1039. http://dx.doi.org/10. 1038/si.bic.6605873.
- Bazin, D., Daudon, M., Combes, C., Rey, C., 2012. Characterization and some physico-chemical aspects of pathological microcalcifications. Chem. Rev. 112, 5092–5120. http://dx.doi.org/10.1021/cr200068d.
- Ben Lakhdar, A., Daudon, M., Mathieu, M.C., Kellum, A., Balleyguier, C., Bazin, D., 2016. Underlining the complexity of the structural and chemical characteristics of ectopic calcifications in breast tissues through FE-SEM and μFTIR spectroscopy. C. R. Chim. 19, 1610–1624. http://dx.doi.org/10.1016/j.crci.2015.03.011.
- Bergholt, M.S., St-Pierre, J., Offeddu, G.S., Parmar, P.A., Albro, M.B., Puetzer, J.L., Oyen, M.L., Stevens, M.M., 2016. Raman spectroscopy reveals new insights into the zonal organization of native and tissue-engineered articular cartilage. ACS Cent. Sci. 2, 885–895. http://dx.doi.org/10.1021/acscentsci.6b00222.
- Bertazzo, S., Gentleman, E., Cloyd, K.L., Chester, A.H., Yacoub, M.H., Stevens, M.M., 2013. Nano-analytical electron microscopy reveals fundamental insights into human cardiovascular tissue calcification. Nat. Mater. 12, 576–583. http://dx.doi.org/10. 1038/nmat3627.
- Bhargava, R., Madabhushi, A., 2016. Emerging themes in image informatics and molecular analysis for digital pathology. Annu. Rev. Biomed. Eng. 18, 387–412. http://dx.doi.org/10.1146/annurev-bioeng-112415-114722.
- Boskey, A.L., 1989. Noncollagenous matrix proteins and their role in mineralization. Bone Miner. 6, 111–123. http://dx.doi.org/10.1016/0169-6009(89)90044-5.
- Büsing, C.M., Keppler, U., Menges, V., 1981. Differences in microcalcifications in breast tumors. Virchows Arch. A 393, 307–313. http://dx.doi.org/10.1007/BF00430830.
- Chappard, D., Bizot, P., Mabilleau, G., Hubert, L., 2016. Aluminum and bone: Review of new clinical circumstances associated with Al³⁺ deposition in the calcified matrix of bone. Morphologie 100, 95–105. http://dx.doi.org/10.1016/j.morpho.2015.12.001.
- Chen, J., Peacock, J.R., Branch, J., Merryman, D.W., 2015. Biophysical analysis of dystrophic and osteogenic models of valvular calcification. J. Biomech. Eng. 137, 20903. http://dx.doi.org/10.1115/1.4029115.
- Cheng, J.X., Sie, X.S., 2015. Vibrational spectroscopic imaging of living systems: an emerging platform for biology and medicine. Science 350, aaa8870. http://dx.doi. org/10.1126/science.aaa8870.
- Choi, S., Coonrod, S., Estroff, L.A., Fischbach, C., 2015. Chemical and physical properties of carbonated hydroxyapatite affect breast cancer cell behavior. Acta Biomater. 24, 333–342. http://dx.doi.org/10.1016/j.actbio.2015.06.001.
- Cox, R.F., Morgan, M.P., 2013. Microcalcifications in breast cancer: lessons from physiological mineralization. Bone 53, 437–450. http://dx.doi.org/10.1016/j.bone. 2013.01.013.
- Cuscó, R., Guitián, F., de Aza, S., Artús, L., 1998. Differentiation between hydroxyapatite and β -tricalcium phosphate by means of μ -Raman spectroscopy. J. Eur. Ceram. Soc. 18, 1301–1305. http://dx.doi.org/10.1016/S0955-2219(98)00057-0.
- De Yoreo, J.J., Gilbert, P.U.P.A., Sommerdijk, N.A.J.M., Penn, R.L., Whitelam, S., Joester, D., Zhang, H., Rimer, J.D., Navrotsky, A., Banfield, J.F., Wallace, A.F., Michel, F.M., Meldrum, F.C., Colfen, H., Dove, P.M., 2015. Crystallization by particle attachment in synthetic, biogenic, and geologic environments. Science 349, aaa6760. http://dx.doi.org/10.1126/science.aaa6760.
- Esserman, L., Yau, C., 2015. Rethinking the standard for ductal carcinoma in situ treatment. JAMA Oncol. 1, 881–883. http://dx.doi.org/10.1001/jamaoncol.2015.2510.5.
- Ferranti, C., De Yoldi, G.C., Biganzoli, E., Bergonzi, S., Mariani, L., Scaperrotta, G., Marchesini, M., 2000. Relationships between age, mammographic features, and pathological tumour characteristics in non-palpable breast cancer. Br. J. Radiol. 73, 698–705. http://dx.doi.org/10.1259/bjr.73.871.11089459.
- Fleet, M.E., 2013. The carbonate ion in hydroxyapatite: recent X-ray and infrared results. Front. Biosci. (Elite Ed) 5, 643–652. http://dx.doi.org/10.2741/E645.
- Frappart, L., Boudeulle, M., Boumendil, J., Lin, H.C., Martinon, I., Palayer, C., Mallet-Guy, Y., Raudrant, D., Bremond, A., Rochet, Y., 1984. Structure and composition of microcalcifications in benign and malignant lesions of the breast: study by light microscopy, transmission and scanning electron microscopy, microprobe analysis, and X-ray diffraction. Hum. Pathol. 15, 880–889. http://dx.doi.org/10.1016/S0046-8177(84)80150-1.
- Frappart, L., Remy, I., Lin, H., Bremond, A., 1986. Different types of microcalcifications observed in breast pathology. Virchows Arch. A 410, 179–187. http://dx.doi.org/10. 1007/BF00710823.
- Gal, A., Kahil, K., Vidavsky, N., Devol, R.T., Gilbert, P.U.P.A., Fratzl, P., Weiner, S.,

- Addadi, L., 2014. Particle accretion mechanism underlies biological crystal growth from an amorphous precursor phase. Adv. Funct. Mater. 24, 5420–5426. http://dx.doi.org/10.1002/adfm.201400676.
- Gal, A., Weiner, S., Addadi, L., 2015. A perspective on underlying crystal growth mechanisms in biomineralization: solution mediated growth versus nanosphere particle accretion. CrystEngComm 17, 2606–2615. http://dx.doi.org/10.1039/C4CE01474J.
- Galkin, B.M., Frasca, P., Feig, S.A., Holderness, K.E., 1982. Non-calcified breast particles: a possible new marker of breast cancer. Invest. Radiol. 17, 119–128. http://dx.doi. org/10.1097/00004424-198203000-00002.
- Gupta, P.K., Majumder, S.K., 1997. Breast cancer diagnosis using N2 laser excited auto-fluorescence spectroscopy. Lasers Surg. Med. 21, 417–422. http://dx.doi.org/10. 1002/(SICI)1096-9101(1997)21:5 < 417::AIDLSM2> 3.0.CO;2-T.
- Haka, A., Shafer-Peltier, K., Fitzmaurice, M., Crowe, J., Dasari, R.R., Feld, M.S., 2002. Identifying microcalcifications in benign and malignant breast lesions by probing differences in their chemical composition using Raman spectroscopy. Cancer Res. 62, 5275-5290
- Hassler, O., 1969. Microradiographic investigations of calcifications of the female breast. Cancer 23, 1103–1109. http://dx.doi.org/10.1002/1097-0142(196905) 23:5 < 1103::AID-CNCR2820230514 > 3.0.CO;2-7.
- Hendley, C.T., Tao, J., Kunitake, J.A.M.R., De Yoreo, J.J., Estroff, L.A., 2015. Microscopy techniques for investigating the control of organic constituents on biomineralization. MRS Bull. 40, 480–489. http://dx.doi.org/10.1557/mrs.2015.98.
- Hoda, S.A., Brogi, E., Koerner, F.C., Rosen, P.P., 2014. Rosen's Breast Pathology, fourth ed. Lippincott Williams & Wilkins, Philadelphia.
- Holland, R., Hendriks, J.H.C.L., 1994. Microcalcifications associated with ductal carcinoma in situ: mammographic-pathologic correlation. Semin. Diagn. Pathol. 11, 181–192.
- Hovden, R., Wolf, S.E., Holtz, M.E., Marin, F., Muller, D.A., Estroff, L.A., 2015. Nanoscale assembly processes revealed in the nacroprismatic transition zone of Pinna nobilis mollusc shells. Nat. Commun. 6, 10097. http://dx.doi.org/10.1038/ncomms10097.
- Hutcheson, J.D., Goettsch, C., Bertazzo, S., Maldonado, N., Ruiz, J.L., Goh, W., Yabusaki, K., Faits, T., Bouten, C., Franck, G., Quillard, T., Libby, P., Aikawa, M., Weinbaum, S., Aikawa, E., 2016. Genesis and growth of extracellular-vesicle-derived microcalcification in atherosclerotic plaques. Nat. Mater. 15, 335–343. http://dx.doi.org/10.1038/nmat4519.
- Kim, K.M., 1995. Apoptosis and calcification. Scanning Microsc. 9, 1137-1178.
- Kneipp, J., Schut, T.B., Kliffen, M., Menke-Pluijmers, M., Puppels, G., 2003. Characterization of breast duct epithelia: a Raman spectroscopic study. Vib. Spectrosc. 32, 67–74. http://dx.doi.org/10.1016/S0924-2031(03)00048-1.
- Koboldt, D.C., et al., 2012. Comprehensive molecular portraits of human breast tumours. Nature 490, 61–70. http://dx.doi.org/10.1038/nature11412.
- Lagier, R., Baud, C., 2003. Magnesium whitlockite, a calcium phosphate crystal of special interest in pathology. Pathol. Res. Pract. 199, 329–335. http://dx.doi.org/10.1078/ 0344-0338-00425.
- Mannello, F., Ligi, D., Canale, M., 2013. Aluminium, carbonyls and cytokines in human nipple aspirate fluids: possible relationship between inflammation, oxidative stress and breast cancer microenvironment. J. Inorg. Biochem. 128, 250–256. http://dx. doi.org/10.1016/j.jinorgbio.2013.07.003.
- Marusyk, A., Almendro, V., Polyak, K., 2012. Intra-tumour heterogeneity: a looking glass for cancer? Nat. Rev. Cancer 12, 323–334. http://dx.doi.org/10.1038/nrc3261.
- Mohler, E.R., Gannon, F., Reynolds, C., Zimmerman, R., Keane, M.G., Kaplan, F.S., 2001. Bone formation and inflammation in cardiac valves. Circulation 103, 1522–1528. http://dx.doi.org/10.1161/01.CIR.103.11.1522.
- Ng, K.H., Looi, L.M., Bradley, D.A., 1997. The elemental composition of breast tissue: can this be related to breast particle deposition? J. Radioanal. Nucl. Chem. 217, 193–199. http://dx.doi.org/10.1007/BF02034442.
- Nguyen, K., Holtz, M., Muller, D., 2013. AirSEM: electron microscopy in air, without a specimen chamber. Microsc. Microanal. 19, 428–429. http://dx.doi.org/10.1017/S1431927613004133.
- Nguyen, K.X., Holtz, M.E., Richmond-Decker, J., Muller, D.A., 2016. Spatial resolution in scanning electron microscopy and scanning transmission electron microscopy without a specimen vacuum chamber. Microsc. Microanal. 22, 754–767. http://dx. doi.org/10.1017/S1431927616011405.
- Olafson, K.N., Ketchum, M.A., Rimer, J.D., Vekilov, P.G., 2015. Mechanisms of hematin crystallization and inhibition by the antimalarial drug chloroquine. Proc. Natl. Acad. Sci. U.S.A. 112, 4946–4951. http://dx.doi.org/10.1073/pnas.1501023112.
- Pathi, S.P., Lin, D.D.W., Dorvee, J.R., Estroff, L.A., Fischbach, C., 2011. Hydroxyapatite nanoparticle-containing scaffolds for the study of breast cancer bone metastasis.

- Biomaterials 32, 5112–5122. http://dx.doi.org/10.1016/j.biomaterials.2011.03.055. Penel, G., Leroy, G., Rey, C., Bres, E., 1998. MicroRaman spectral study of the PO₄ and CO₃ vibrational modes in synthetic and biological apatites. Calcif. Tissue Int. 63, 475–481
- Poggi, S., Skinner, H., Ague, J., Carter, D., 1998. Using scanning electron microscopy to study mineral deposits in breast tissues. Am. Minerol. 83, 1122–1126.
- Poloni, L.N., Ward, M.D., 2014. The materials science of pathological crystals. Chem. Mater. 26, 477–495. http://dx.doi.org/10.1021/cm402552v.
- Radi, M., 1989. Calcium oxalate crystals in breast biopsies. Arch. Pathol. Lab. Med. 113, 1367–1369.
- Rimer, J.D., An, Z., Zhu, Z., Lee, M.H., Goldfarb, D.S., Wesson, J.A., Ward, M.D., 2010. Crystal growth inhibitors for the prevention of L-cystine kidney stones through molecular design. Science 330, 337–341. http://dx.doi.org/10.1126/science.1191968.
- Schaeberle, M.D., Kalasinsky, V.F., Luke, J.L., Lewis, E.N., Levin, I.W., Treado, P.J., 1996.
 Raman chemical imaging: histopathology of inclusions in human breast tissue. Anal.
 Chem. 68, 1829–1833.
- Scimeca, M., Giannini, E., Antonacci, C., Pistolese, C.A., Spagnoli, L.G., Bonanno, E., 2014. Microcalcifications in breast cancer: an active phenomenon mediated by epithelial cells with mesenchymal characteristics. BMC Cancer 14, 286. http://dx.doi. org/10.1186/1471-2407-14-286.
- Scott, R., Kendall, C., Stone, N., Rogers, K., 2017. Elemental vs. phase composition of breast calcifications. Sci. Rep. 7, 136. http://dx.doi.org/10.1038/s41598-017-00183-y
- Scott, R., Stone, N., Kendall, C., Geraki, K., Rogers, K., 2016. Relationships between pathology and crystal structure in breast calcifications: an in situ X-ray diffraction study in histological sections. npj Breast Cancer 2, 16029. http://dx.doi.org/10.1038/npjbcancer.2016.29.
- Shafer-Peltier, K.E., Haka, A.S., Fitzmaurice, M., Crowe, J., Myles, J., Dasari, R.R., Feld, M.S., 2002. Raman microspectroscopic model of human breast tissue: implications for breast cancer diagnosis in vivo. J. Raman Spectrosc. 33, 552–563. http://dx.doi.org/10.1002/jts.877.
- Sharma, T., Radosevich, J.A., Pachori, G., Mandal, C.C., 2016. A molecular view of pathological microcalcification in breast cancer. J. Mammary Gland Biol. Neoplasia 21, 25–40. http://dx.doi.org/10.1007/s10911-015-9349-9.
- Solomonov, I., Talmi-Frank, D., Milstein, Y., Addadi, S., Aloshin, A., Sagi, I., 2014. Introduction of correlative light and airSEM™ microscopy imaging for tissue research under ambient conditions. Sci. Rep. 4, 1–7. http://dx.doi.org/10.1038/srep05987.
- Surmacki, J., Musial, J., Kordek, R., Abramczyk, H., 2013. Raman imaging at biological interfaces: applications in breast cancer diagnosis. Mol. Cancer 12, 1–13.
- Tanizawa, Y., Sawamura, K., Suzuki, T., 1990. Reaction characteristics of dental and synthetic apatites with Al³⁺ and La³⁺ ions in acidic solutions. J. Chem. Soc. Faraday Trans. 86, 4025–4029. http://dx.doi.org/10.1039/ft9908604025.
- Tse, G.M., Tan, P.-H., Pang, A.L.M., Tang, A.P.Y., Cheung, H.S., 2008. Calcification in breast lesions: pathologists' perspective. J. Clin. Pathol. 61, 145–151.
- Vidavsky, N., Addadi, S., Mahamid, J., Shimoni, E., Ben-Ezra, D., Shpigel, M., Weiner, S., Addadi, L., 2014. Initial stages of calcium uptake and mineral deposition in sea urchin embryos. Proc. Natl. Acad. Sci. U.S.A. 111, 39–44. http://dx.doi.org/10.1073/pngs_1312833110
- Vidavsky, N., Addadi, S., Schertel, A., Ben-Ezra, D., Shpigel, M., Addadi, L., Weiner, S., 2016. Calcium transport into the cells of the sea urchin larva in relation to spicule formation. Proc. Natl. Acad. Sci. 113, 12637–12642. http://dx.doi.org/10.1073/ pnas.1612017113.
- Wang, Z., Hauser, N., Singer, G., Trippel, M., Kubik-Huch, R.A., Schneider, C.W., Stampanoni, M., 2014. Non-invasive classification of microcalcifications with phasecontrast X-ray mammography. Nat. Commun. 5, 3797. http://dx.doi.org/10.1038/ promps4797
- Waychunas, G.A., 2002. Apatite luminescence. Rev. Mineral. Geochemistry 48, 701–742. http://dx.doi.org/10.2138/rmg.2002.48.19.
- Weiner, S., Addadi, L., 2011. Crystallization pathways in biomineralization. Annu. Rev.
 Mater. Res. 41, 21–40. http://dx.doi.org/10.1146/annurev-matsci-062910-095803.
 Wilkinson, L., Thomas, V.A.L., Sharma, N., 2017. Microcalcification on mammography:
- Wilkinson, L., Thomas, V.A.L., Sharma, N., 2017. Microcalcification on mammography: approaches to interpretation and biopsy. Br. J. Radiol. 90, 20160594. http://dx.doi. org/10.1259/bjr.20160594.
- Zipfel, W.R., Williams, R.M., Christie, R., Nikitin, A.Y., Hyman, B.T., Webb, W.W., 2003. Live tissue intrinsic emission microscopy using multiphoton-excited native fluorescence and second harmonic generation. Proc. Natl. Acad. Sci. 100, 7075–7080. http://dx.doi.org/10.1073/pnas.0832308100.